Measurements of magnetic field fluctuations in TJ-II plasmas with new in-vessel helical arrays of magnetic coils

E. Ascasíbar[1], F. Lapayese[1], A. Soleto[1], A. Jiménez-Denche[1], Á. Cappa[1], P. Pons-Villalonga[1], A. B. Portas[1], G. Martín[1], J.M. Barcala[2], R. García-Gómez[1], M. Chamorro[1], L. Cebrián[1], R. Antón[1], L. Bueno[1], C. Reynoso[1], V. Guisse[1], A. López-Fraguas[1] and the TJ-II team

[1] Laboratorio Nacional de Fusión. CIEMAT, 28040 Madrid, Spain
[2] Departamento de Tecnología. CIEMAT, 28040 Madrid, Spain

E-mail: enrique.ascasibar@ciemat.es

Abstract. This paper describes two new helical arrays of magnetic coils recently installed inside the TJ-II vacuum vessel. Their main objective is the precise measurement of the spatial periodicity of the magnetohydrodynamic (MHD) perturbations usually found in the TJ-II plasmas. Given the high probability of coil failures due to the harsh plasma environment and in view of the extremely difficult access to the TJ-II vessel interior for maintenance, the coil system has been divided in two quasi-identical helical arrays. Both arrays consists of 32 triaxial sensors measuring orthogonal components of the local magnetic field along an ideal helical path whose trajectory run close to the plasma edge. A description of the main characteristics of coils and arrays as well as their nominal positioning along an ideal helical path, inside the vessel, is given. A precise experimental determination of the real spatial orientation of the coils is performed by comparing the signals measured in current ramp-up and ramp-down experiments with calculations based on a filamentary model for the TJ-II magnetic coils. After this fine calibration procedure it is possible to analyse the dependence of the amplitude of the measured magnetic field and its fluctuations as a function of the coil distance to the last closed flux surface. The study of the phase evolution of the parallel and perpendicular oscillatory components is also enabled. Finally two examples of mode number determination are shown. One corresponds to a low frequency mode appearing in pure ECRH plasma and the other one shows several modes observed during combined injection of both co and counter neutral beams and identified as Shear Alfvén Waves.

1. Introduction

The TJ-II stellarator (heliac type, major radius 1.5 m, minor radius $\leq$ 0.22 m, four periods, average magnetic field on axis 0.95 T, plasma volume $\leq$ 1 m^3) is on its third decade of operation. Both ECRH (two gyrotrons, 53.2 GHz, P $\leq$ 300 kW each, suitable

for X2 heating) and NBI heating (two H^0 injectors, E $\leq$ 30 kV, P $\leq$ 600 kW each) can be used to produce and sustain the plasma discharge. Moreover, the interaction of fast ions generated by the NBI system with the complex structure of MHD modes typical of a three-dimensional magnetic field generates different types of Alfvén instabilities that have been investigated and reported in previous papers [1–4]. Among other diagnostics, the arrays of magnetic probes distributed around the plasma play an essential role in determining the frequency, amplitude, periodicity (mode numbers) and polarization of the magnetic fluctuations [5–8].

Three groups of magnetic coils have been installed so far in TJ-II along the years of operation of the device. They have been described in detail elsewhere [1, 9, 10]. Two of them are straight sets, located at toroidal planes $\phi = 142^\circ$ and $\phi = 208^\circ$, with 12 coils each, which measure the three cylindrical components of the magnetic field at four positions along a vertical line over the plasma column. The third is a set of 25 coils located at a fixed toroidal plane ($\phi = 315^\circ$), distributed in poloidal direction and covering an angular range of roughly $3\pi/2$. The latter allows extracting information on the poloidal mode number of the MHD plasma instabilities observed. But, overall, the three existing coil systems located at just three toroidal angles are not enough to provide sufficient information on the toroidal periodicity of the MHD modes.

The new system recently installed spans a full TJ-II magnetic field period, i.e 90 degrees in toroidal direction. It consists of two nominally identical arrays that run helically, in phase with the TJ-II plasma column, along the line that connects the vacuum vessel inner corners shown in figure 1. These corners form in the intersections between the circular portions of the vacuum vessel and the indented region forming a groove. The groove is needed to accommodate the central conductors-which provide most of the poloidal magnetic field component of the device-as close as possible to the plasma column. Thus, the helical path described by the arrays is in phase with the helix described by the TJ-II plasma column. A similar design was also used for the helical Mirnov array installed years ago in the H-1NF heliac [11]. In the TJ-II case described in this work, the good coverage in toroidal direction (2.9 degrees separation between adjacent coils) allows the determination of high toroidal MHD mode numbers. In principle, both arrays provide redundant measurements, which is considered an advantage not only for comparison purposes, but also as a contingency measure in case of individual coil failure.

2. Description of the system

Both arrays consist of 32 sensors, each one of them composed by three individual coils, see figure 2, carefully mounted in order to measure the orthogonal components of the local magnetic field in their common centre.

The final desired system required a series production of 2 $\times$ 32 triaxial sensors, i.e., a total number of 192 properly wound individual coils. After a validation phase of the fabrication and assembly procedure, the design of the triaxial sensor unit ended up in a

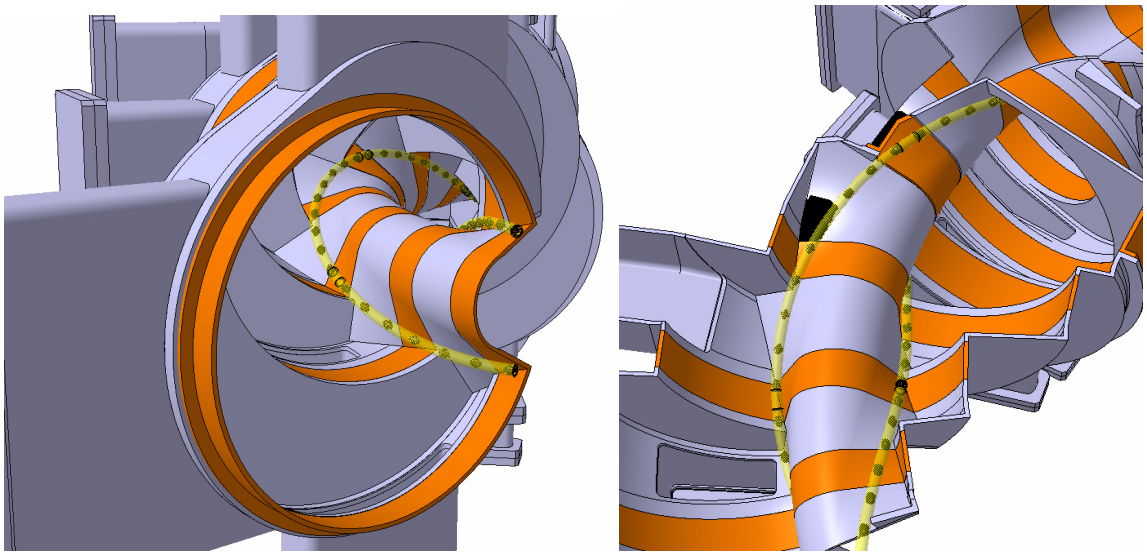

Figure 1. Left: View of the helical trajectory followed by the tubes that support and protect the coils inside the TJ-II vacuum vessel. Right: Top view of the arrangement of the supporting helical tubes. The upper part of the vessel is not drawn.

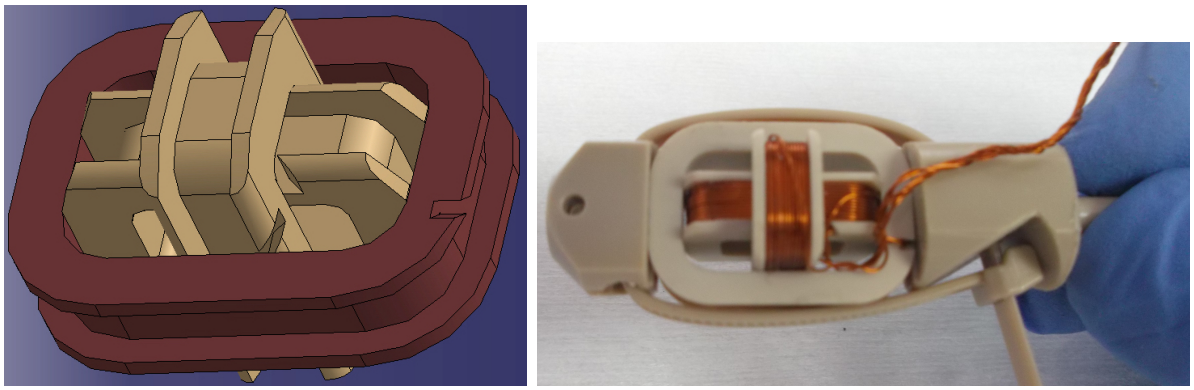

Figure 2. Left: CAD sketch of the final triaxial sensor design showing the three spools (two of them identical) orthogonally arranged, still without the copper wire wound in place. Right: Picture of a prototype sensor.

system composed of two identical coils inserted orthogonally one in another and a third one whose frame is slightly larger and can be finally mounted to become also orthogonal to its two companions, see figure 2. Adjusting properly the number of turns of the third larger coil the sensitivity of the two types of coils became nearly identical, while keeping similar resistance and comparable inductance and capacitance, as seen in table 1 below.

In this way the 3×64 individual coils could be wound in series by an external specialized company on the frames previously machined by another company. The final assembly of the coils inside the protecting tubes and the installation of the full system inside the TJ-II vacuum vessel were done altogether at CIEMAT.

2.1. Coil characteristics

The material chosen for the coil frames has been PEEK polymer due to its excellent mechanical and sliding properties combined with its outstanding wear resistance, very good dimensional stability and low outgassing rate, essential to operate under high vacuum conditions. The material used for winding the coils was Kapton-coated AWG 30 (Φ 0.25 mm) copper wire. Its dipping-applied, uniform Kapton coating provides 2 kV DC insulation, ultra-high vacuum compatibility and operating temperature up to 250°C. After manufacturing, the coils have been tested to discard isolation failures. Table 1 contains the electrical parameters of the two types of individual coils.

Table 1. Electrical parameters of the two types of coils

	size (mm^2)	nr. windings	eff. area (cm^2)	R (Ω)	L (μH)	C (μF)
small	15x8	88, in seven layers	141	3.7	110	10
large	22x15	41, in four layers	141	3.3	37	4

2.2. Inter-sensor elastic couplers. Protective and guiding corrugated tube

The angular separation in toroidal direction between consecutive sensors is fixed, 90/31 $\approx$ 2.9 degrees. Elastic couplers fastening consecutive sensors allow a precise positioning while providing the full system with the required flexibility to follow the desired helical path (see pictures in figure 3). The elastic couplers, though, allow fixing the desired angular position of a given sensor within the sensor train. Thus, to facilitate the interpretation of phase differences measured by adjacent coils, we have imposed to each triaxial sensor a fixed right-handed twist of 360/31 $\approx$ 11.6 degrees respect to its preceding neighbour. In this way, the first and the 32-th sensor have identical nominal position and orientation with respect to the TJ-II magnetic field. This is illustrated later in figure 8 where the result of calculating the position and orientation of the coils in respect to the static field and the plasma is shown.

The external jacket that guides the magnetic coil array and provides protection against plasma is a corrugated AISI316L stainless steel flexible tube with inner diameter 20.5 mm. A longitudinal cut is made along the tube to avoid the induction of eddy currents along the short path and the concomitant reduction in coil frequency bandwidth, see picture in figure 4.

2.3. Installation in the vacuum vessel

The TJ-II inner vacuum vessel groove mentioned in the introduction is covered with shaped detachable stainless steel plates, 2 mm thick, for thermal shielding purposes. Clamps accurately welded to these plates at appropriate locations support the corrugated tubes and define the desired helical path to be followed by the sensor arrays, see pictures in figures 5 and 6. In order to extract the signals out of the vacuum

Figure 3. Top left: arrangement of two magnetic sensors and two elastic couplers Top right: measuring with an inclinometer the required angular twist between adjacent sensors Bottom: train composed of nine triaxial magnetic sensors with their corresponding couplers in between neighbours Note the progressively increasing twist imposed to the sensors.

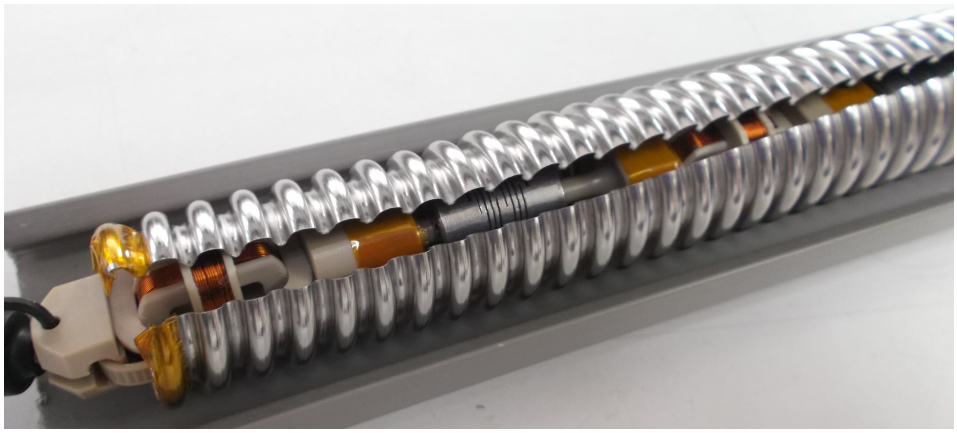

Figure 4. Detail of a portion of the finished sensor train, seen through the cutting machined in the corrugated jacket.

vessel, the 2×192 terminals carrying the voltages measured by the 192 coils are grouped into eight bundles corresponding to sub-arrays with eight triaxial coils each. In turn, bundles corresponding to adjacent sub-arrays are merged, resulting in four groups of bundles that are connected to two identical DN 160 CF feedthrough flanges located in two TJ-II ports, namely D3BOT and D5 SIDE. Figure 6 shows the protecting junctions

used to extract the cable bundles of two of the groups. Each commercial feedthrough flange is equipped with eight DB-25 D-sub connectors, hosting 25 pins each. The five meters distance between both feedthrough flanges and the rack hosting the digitizers in the TJ-II experimental hall is covered by coaxial cables ended in standard BNC connectors.

Figure 5. Left: Assembly tests. Piece of supporting corrugated tube positioned inside a 1:1 scale wooden vacuum vessel mockup. Clamps welded to three shaped protecting plates support and guide the tube along the desired path. Right: Final positioning of both helical arrays inside the TJ-II vacuum vessel. Just the initial parts corrugated tubes, starting at $\phi = 270°$, are seen. The white hanging curved tube is a LED array used for illumination purposes during assembly.

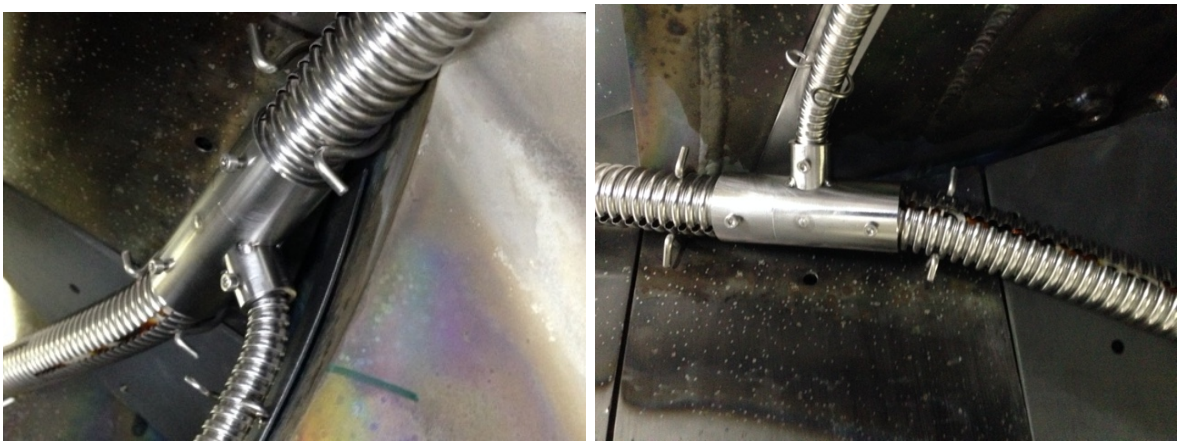

Figure 6. T-junctions to extract the cable bundles corresponding to sub-arrays 1-2 (left picture) and 5-6 (right picture). The thinner corrugated tube protects and guides the cable bundles up to the feedthrough flange located in the D3BOT vacuum vessel port.

2.4. Data acquisition system

Two types of commercial solutions are used to digitize and acquire the measured data. The 96 signals corresponding to the so-called upper helical array are connected to 24 four-channel PCI-DAS4020/12 boards (from Measurement Computing Corporation) logged into six industrial (rugged) IPC-602 PCs. The PCI channels have 12 bits ADC resolution and software-configurable ±1 V or ±5 V input range. The 96 signals of the lower helical array are connected to 6 sixteen-channel PXIe-6368 boards (from National Instruments) logged into a PXIe-1082 PXI Express chassis. The PXI channels have 16 bits ADC resolution and software-configurable ±1 V, ±2 V, ±5 V or ±10 V input range. The typical sampling rate used is 1MS/s for all channels, except when acquiring signals in calibration shots. In this latter case, the full magnetic field pulse, lasting 2.5 seconds, has to be registered and the sampling frequency must be reduced to 0.5 MS/s.

3. Results

3.1. Position and design orientation of each magnetic coil

The nominal position and orientation of the 64 triaxial sensors that compose the two helical arrays are defined by the helical path described by the supporting corrugated tube and the length and twist imposed to the elastic couplers between sensors. The determination of the orthogonal axis system associated to each sensor, where each axis defines the orientation of each different coil within a triaxial sensor, is performed by following the two-step process illustrated in figure 7.

In a first step, if $\vec{r}_c(s)$ is the curve followed by a given array and $\vec{t}(s) \equiv \partial\vec{r}_c/\partial s$ the vector tangent to the curve at every point along the curve, an orthogonal coordinate system, defined by the unit vectors $\vec{T}_i(s)$, $\vec{R}_i(s)$, $\vec{P}_i(s)$, can be associated to the center of every triaxial sensor, where

$$\vec{T}_i(s) = \frac{\vec{t}(s)}{|\vec{t}(s)|} \qquad \vec{R}_i(s) = \frac{\vec{T}_i(s) \times \vec{z}}{|\vec{T}_i(s) \times \vec{z}|} \qquad \vec{P}_i(s) = \vec{T}_i(s) \times \vec{R}_i(s). \tag{1}$$

In these definitions, $\vec{z}$ is the vertical direction. At this stage, the $\vec{R}_i$ and $\vec{P}_i$ vectors still lie in horizontal and vertical planes respectively, as shown in the upper plot of figure 7. Then, in a second step, each coordinate system is rotated around $\vec{T}_i$ by an angle of 360/31 degrees, consistently with the twist imposed during manufacturing. The result is shown in the lower plot of figure 7. For a better understanding of the sensors position and orientation in respect to the plasma, the central position of each array is shown in figure 8 for six given toroidal angles taken along one period of the device. Flux surfaces and field intensity map are those of the standard TJ-II magnetic configuration. The projections of $\vec{R}_d$ and $\vec{P}_d$ – the rotated $\vec{R}_i$ and $\vec{P}_i$ vectors – on each toroidal plane are given as well as the direction of the poloidal component of the magnetic field ($B_p \equiv (B_r^2 + B_z^2)^{\frac{1}{2}}$) The array that has positive z at $\phi = 270°$ is the *upper* array while we will refer to the other array as the *lower* array. This is only for naming

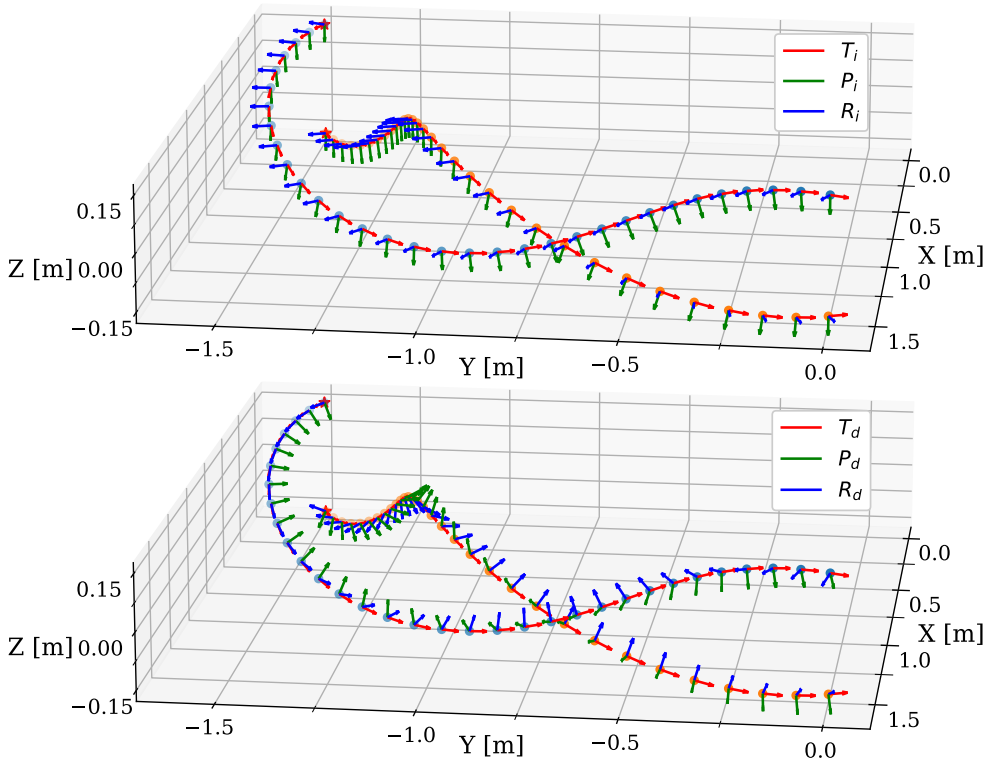

Figure 7. The upper panel shows the nominal orientation of the coils in case of no twist applied to the sensors around the tangential direction. The final nominal position and orientation of the orthogonal coordinate system associated to each triaxial sensor is shown in the lower panel.

purposes since the 3D excursion of both arrays make them explore regions above and below the horizontal plane of the device, as shown in figure 7.

While 'T' indicates the direction tangential to the curve described by each array and therefore the 'T' coils measure the field along this direction, 'R' and 'P' stand for radial and poloidal respectively since, as it is shown in figure 8, the perturbations to the poloidal static field along the radial direction (taking the origin at the plasma center) will impact primarily the signal measured by the 'R' coils.

3.2. Comparing the total measured field to the theoretical equilibrium field

The flat-top magnetic field at any given position of the TJ-II vacuum vessel can be accurately calculated using the model that describes the TJ-II coils [12]. On the other hand, the integration of the signals recorded by the individual coils during the ramp-up of the configuration currents in a TJ-II shot yields the corresponding total measured magnetic flux. Since the effective areas of the coils are known, the vacuum equilibrium magnetic field measured at each location can be compared to the corresponding values of the theoretical field calculated at the center of every triaxial sensor. Needless to say that this comparison is meaningful only if a constant value of the magnetic field over the coil surface can be assumed. This is indeed the case due to the relatively small

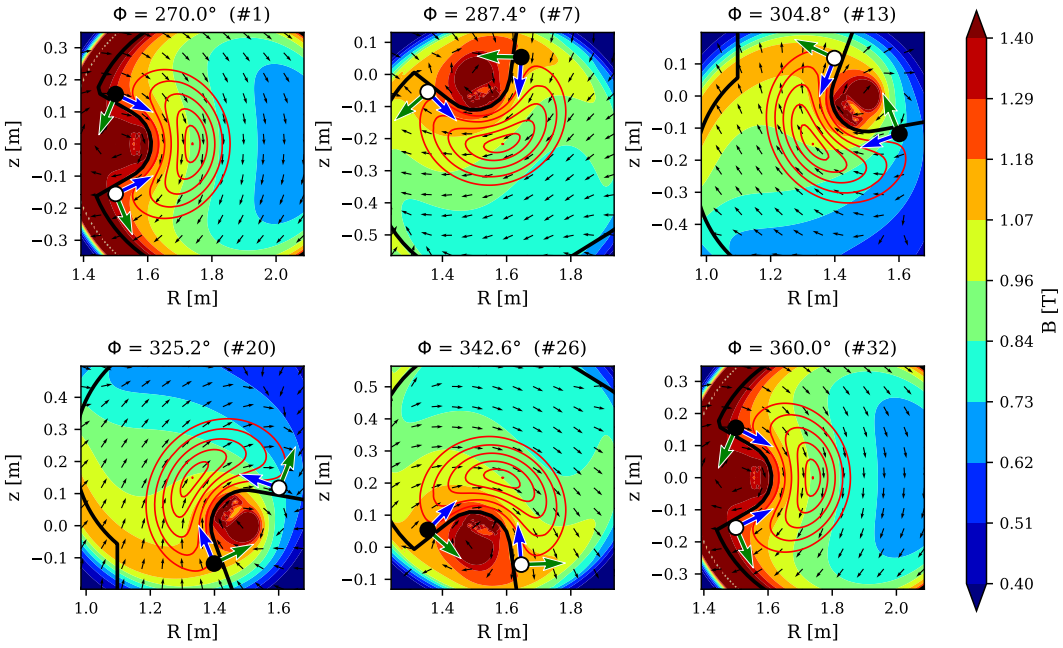

Figure 8. Central position of the upper (black closed circles) and lower (open circles) arrays and projection of $\vec{R}_d$ (in blue) and $\vec{P}_d$ (in green) on the toroidal plane. The direction of the poloidal field component is represented with black arrows. Flux surfaces (red lines) and magnetic field intensity are plotted for reference.

dimensions of the coils and the relatively low magnetic field gradient along the path followed by the arrays. To reduce statistical errors the signals of nine identical TJ-II discharges (51337-51345) have been averaged.

Figure 9 compares the module of the measured magnetic field at the center of each triaxial sensor with the corresponding calculated value, for both helical arrays. It must be noted that, out of the 192 individual coils, six of them (five from the upper array and one from the lower array; see figure 9) were out of order during the calibration shots. This is the reason why only 58 (out of 64) experimental points are displayed, showing an excellent agreement with the calculation. The reproducibility of the measurements is very good and the error bars accounting for their dispersion are smaller than the size of the markers. The eight toroidal field coils per period of the TJ-II configuration produce a noticeable magnetic field ripple. This comparison was done for the standard magnetic configuration illustrated in figure 8.

3.3. Experimental determination of the coils spatial orientation

The result shown in figure 9 confirms that the spatial location of each set of coils is given by its design values to a reasonable degree of accuracy. The final orientation of each coil and the deviations from the design values, given by $\vec{R}_d, \vec{P}_d$ and $\vec{T}_d \equiv \vec{T}_i$, must be experimentally determined after the installation, as the deformation in the elastic couplers between sensors due to the curved path of the sensor train can induce

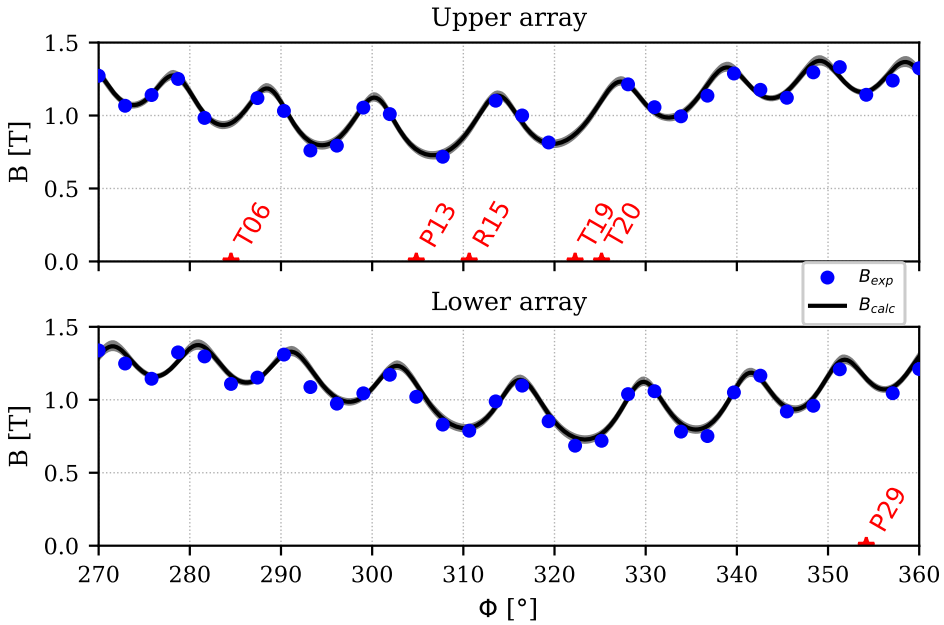

Figure 9. Comparison between the measured module of the local static magnetic field at the nominal position of the triaxial sensors centres (blue dots) and the calculated value of the magnetic field along the nominal path of the helical arrays (black curves), for both arrays. Red stars distributed along the coordinates axis indicate the nominal positions of the coils whose signal was missing during the measurement (also indicated). The horizontal axis corresponds to the toroidal position of each triaxial sensor.

additional rotations in each tri-axial group. Furthermore, there is an additional degree of freedom in the polarity of each individual sensor, that depends on its wiring and must be corrected in order to measure unambiguously the relative phases between coil signals and the temporal and spatial periodicity of the observed modes.

For this purpose, four different current ramp-up and ramp-down sequences in the main field coils of the device were used (figure 10) in order to obtain a variable field at the sensor positions.

The magnetic field applied to the center of each sensor can be calculated to a reasonable precision using a filamentary model of the TJ-II magnetic coils, given the currents that go through them. Finding an orthogonal transformation between the components of the magnetic field in cartesian coordinates calculated with this model and the ones measured by the sensors is an orthogonal Procrustes problem [13], for which a solution using singular value decomposition has been implemented.

For each set of coils, consider the $3 \times n$ matrices B_{exp} and B_{th}, given by the column vectors $\{\vec{B}^i_{\text{exp}}\}$ and $\{\vec{B}^i_{\text{th}}\}$ that correspond to the magnetic field at instant i, experimentally measured by the triaxial sensor in the first case and calculated from the field currents in cartesian coordinates in the second one. We want to find the orthogonal transformation M that, applied to this particular set, minimizes:

$$M = \underset{X}{\text{argmin}} \left(\sum_i \left| X\vec{B}^i_{\text{exp}} - \vec{B}^i_{\text{th}} \right|^2 \right) \tag{2}$$

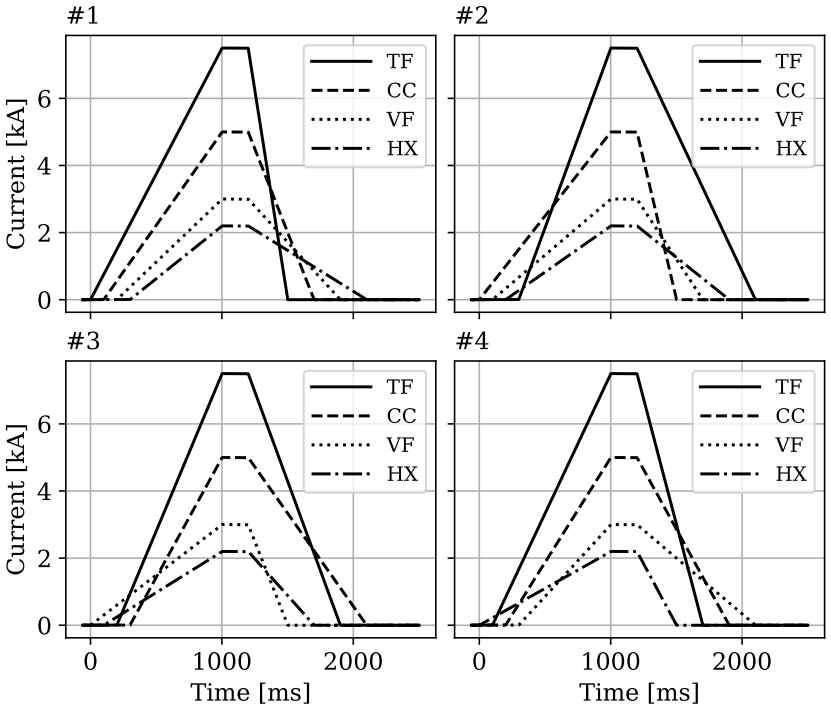

Figure 10. Current waveforms used in the calibration shots. TF, CC, VF, and HX are the currents in the toroidal, central, vertical and helical conductors of the device, respectively.

It can be shown [14] that, if

$$B_{\text{exp}} B_{\text{th}}^T = U \Sigma V^T \tag{3}$$

is the singular value decomposition of the 3×3 cross-covariance matrix $B_{\text{exp}} B_{\text{th}}^T$, the orthogonal transformation M that aligns $M B_{\text{exp}}$ with B_{th} in the least squares sense, and therefore minimizes the term on the RHS of equation 2, is given by:

$$M = V U^T \tag{4}$$

This orthogonal matrix M can be either a rotation or a reflection matrix, depending on the handedness defined by the wiring of the triaxial sensors. If B_{th} is expressed in the cartesian coordinate system, the columns of M are the final vectors $\vec{T}$, $\vec{P}$ and $\vec{R}$ that give the real orientations of the probes. The results of this calibration are shown in figure 11. As expected, most deviations from the design orientations are small. Moreover, the calibration experiments have been essential to identify a group of sensors for which the R and P labels were accidentally switched during installation. These are represented by green triangles in figure 11.

3.4. Raw data and magnetic fluctuations spectrogram

As a first example, the raw data of one of the signals measured by the 'P' coils and its spectrogram calculated with the Short Time Fourier Transform (STFT) algorithm, are

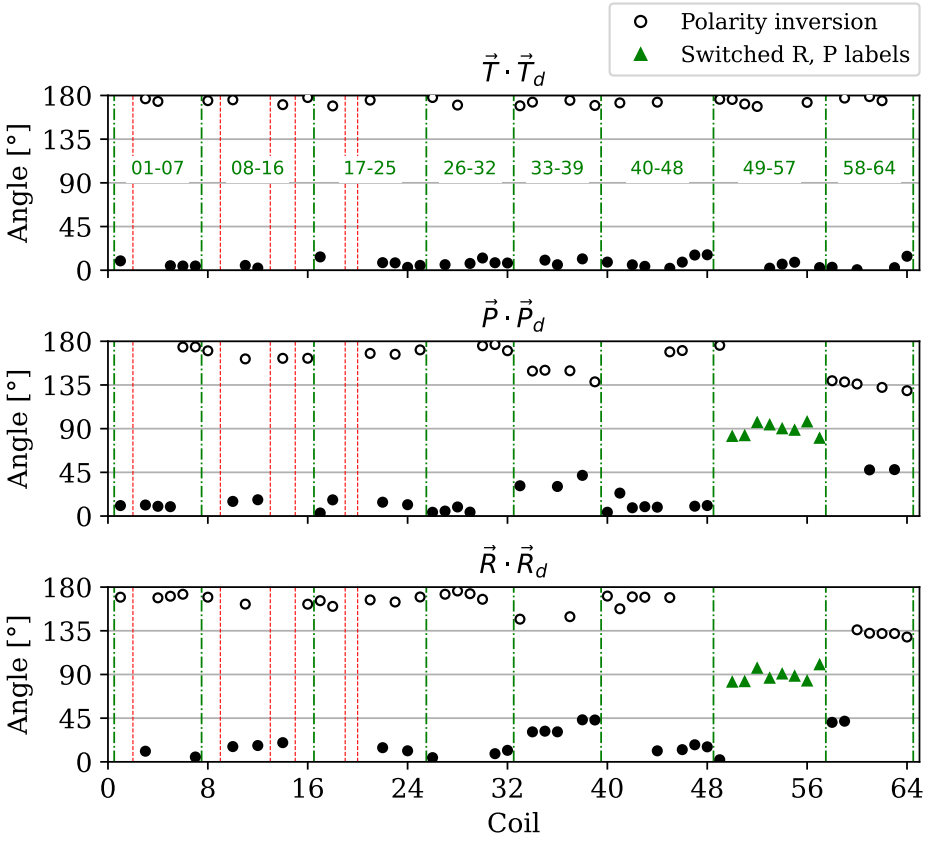

Figure 11. Relative angle between the design orientation vectors and the vectors determined from the calibration experiments.

shown in figure 12. In this case, a low frequency mode appearing in pure ECRH plasma has been chosen to illustrate the capabilities of the diagnostic.

The information about the spatial structure of the perturbation contained in the raw data is better understood in terms of the total amplitude of the perturbed field ($|\delta\vec{B}|$) and the projections of $\delta\vec{B}$ along the directions parallel and perpendicular to the static field $\vec{B}_0$. The total perturbed field can be written in either of these two ways:

$$\delta\vec{B} = \delta B_{\parallel}\hat{b} + \delta\vec{B}_{\perp} = \delta B_R\vec{R} + \delta B_P\vec{P} + \delta B_T\vec{T} \tag{5}$$

where $\hat{b} \equiv \vec{B}_0/|\vec{B}_0|$ and $\delta B_R(t)$, $\delta B_P(t)$ and $\delta B_T(t)$ are the perturbed field amplitudes measured by each of the 'R', 'P', 'T' coils respectively. Therefore, the parallel and perpendicular components of the perturbation can be defined as:

$$\delta B_{\parallel} = \delta\vec{B}\cdot\hat{b} = \delta B_R(\vec{R}\cdot\hat{b}) + \delta B_P(\vec{P}\cdot\hat{b}) + \delta B_T(\vec{T}\cdot\hat{b}) \tag{6}$$

$$\delta\vec{B}_{\perp} = \delta\vec{B} - \delta B_{\parallel}\hat{b} \tag{7}$$

The perpendicular component of the perturbation can be written in terms of the polarization basis vectors as

$$\delta\vec{B}_{\perp} = \delta B_{\perp,1}\vec{e}_1 + \delta B_{\perp,2}\vec{e}_2 \tag{8}$$

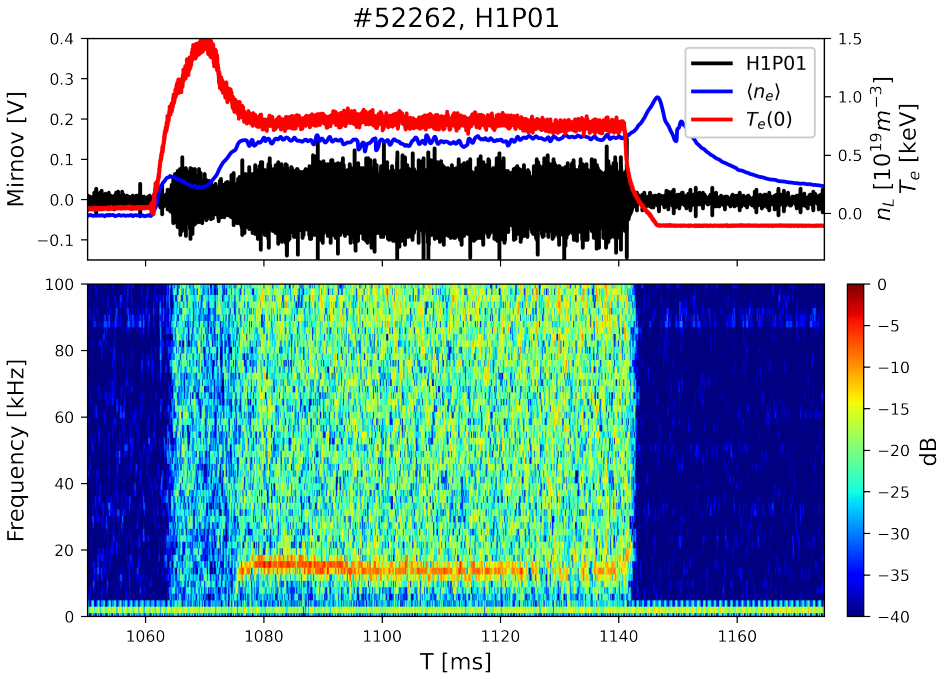

Figure 12. On top, the raw time signal of one of the upper array coils together with the line density (blue line) and the central electron temperature (red line). The spectrogram of magnetic fluctuations is shown in the bottom panel.

were

$$\vec{e}_1 \equiv \frac{\hat{b} \times \vec{R}_d}{|\hat{b} \times \vec{R}_d|} \tag{9}$$

$$\vec{e}_2 \equiv \vec{e}_1 \times \hat{b} \tag{10}$$

Defining $\vec{e}_1$ perpendicular to $\vec{R}_d$ (or $\vec{P}_d$ alternatively) makes the basis vector rotate following the helical excursion of the plasma column. Building these quantities from the originally measured ones provides insight into the mode polarization properties by separating the perpendicular field oscillations (which, for instance, are typical of a shear Alfvén wave) from the ones parallel to $\vec{B}_0$. We can calculate the envelope of the oscillations by taking the absolute value of the Hilbert transform of the raw signals, band-pass filtered around the mode frequency, as it is shown in figure 13. This information will be useful when studying the dependence of the perturbed field amplitude on the distance from the sensor location to the plasma. One of the oscillatory components perpendicular to the magnetic field ($\delta B_{\perp,2}$), evaluated from the lower array measurements, is shown in figure 14. The signals have been normalized to easily visualize the phase difference between them.

The analysis presented in figures 13 and 14 has been performed for the mode pictured in figure 12, filtered between 10 and 30 kHz in the interval 1090 ms $< t <$ 1100 ms.

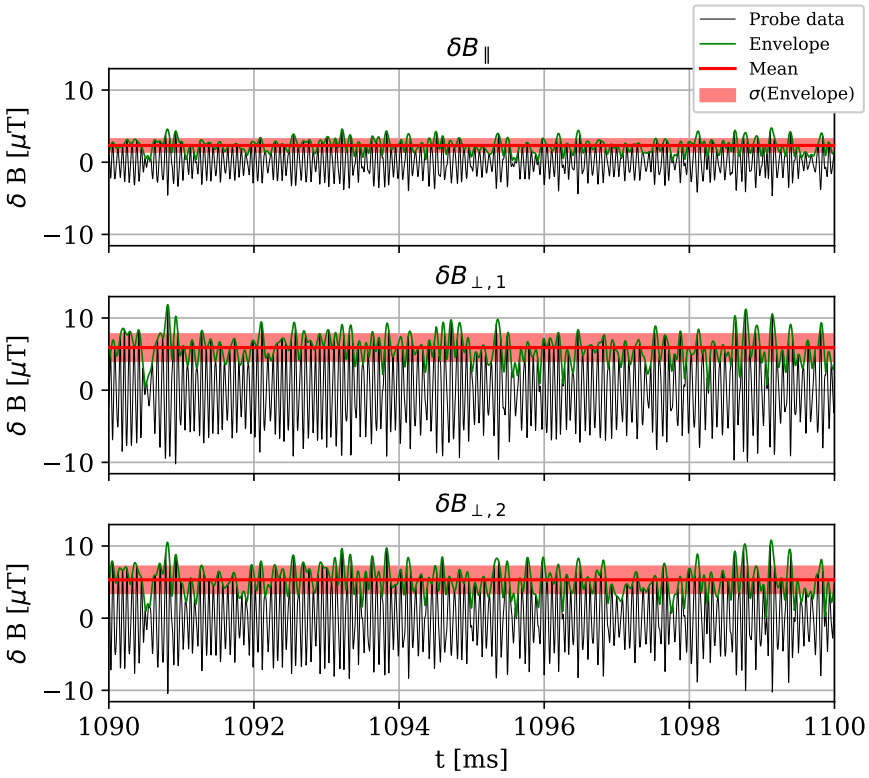

Figure 13. Decomposition of the signal measured by the first set of coils in the upper array in its parallel and perpendicular components. Signals envelope (green line) and their corresponding mean value (red line) and standard deviation (shaded red area) are shown.

3.5. Mode number determination

To measure the periodicity (mode numbers) of a perturbation of frequency ω we need first an estimation of the position of the sensors in magnetic coordinates, those in which the mode structure can be expressed in its simpler form, and which is commonly given by

$$\delta\vec{B}_{tot}(\rho,\vartheta,\varphi,t) = \Re\left[\sum_{m,n}\delta\vec{B}_{m,n}(\rho)e^{i(m\vartheta+n\varphi-\omega t)}\right]. \tag{11}$$

In expression 11, φ and ϑ are the angles in magnetic coordinates, usually Boozer coordinates, n and m are the toroidal and the poloidal mode numbers respectively and $\rho \equiv \sqrt{\psi}$, being ψ the normalized toroidal flux. The radial eigenfunctions (complex scalar amplitudes $\delta\vec{B}_{m,n}(\rho)$) take into account the phase difference between modes with same frequency and different mode numbers that for instance may be encountered when gap modes belonging to the shear Alfvén waves spectrum are considered [4].

To determine the magnetic coordinates corresponding to the position of each set of triaxial coils, each set location has been mapped to its closest position to the plasma. The corresponding values of the magnetic angles for this position have been calculated with the BOOZ_XFORM code using the output of a VMEC vacuum equilibrium. The

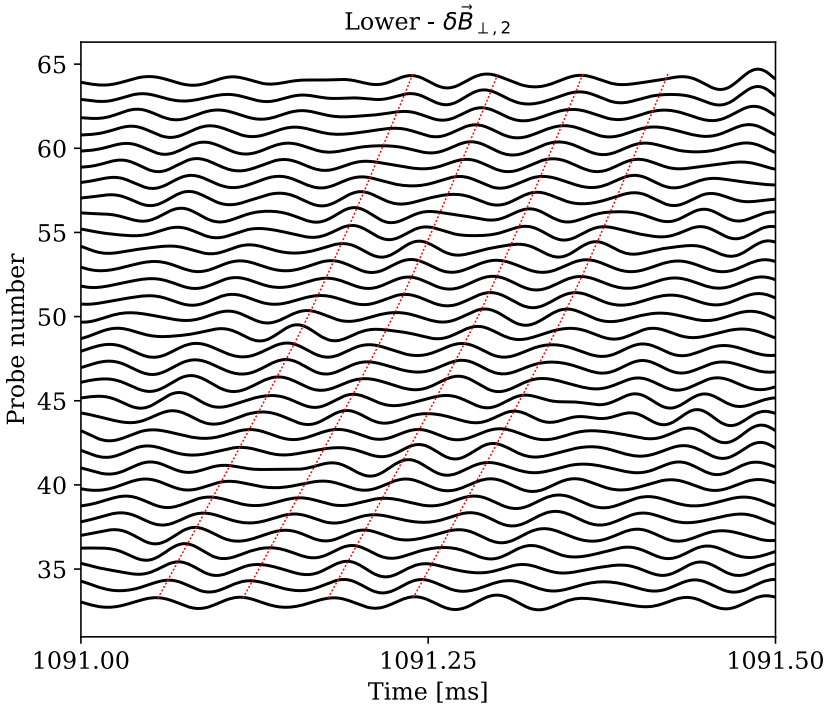

Figure 14. Normalized $\delta B_{\perp,2}$ measured by the lower array for the mode shown in figure 12.

result is shown in figure 15 for the two triaxial arrays and also for the poloidal array. The precise mapping actually depends slightly on the real plasma equilibrium whether is it modified by plasma pressure or by the plasma current produced by the different non inductive current sources (i.e. bootstrap, ECCD (Electron Cyclotron Current Drive) or NBCD (Neutral Beam Current Drive)).

When measuring the poloidal mode number with detectors distributed in a vertical plane of the device, the angle φ can be considered approximately constant (see figure 15) and usual two-dimensional FFT analysis [10, 15] for probes equally spaced in ϑ or singular value decomposition (SVD) of the data matrix [1, 16] have been used to provide an estimation of the poloidal mode number. However, because of the plasma helicity, an array of probes installed along the toroidal direction of the device will provide measurements that depend equally on the toroidal and the poloidal mode number of the underlying perturbation and numerical tools specifically adapted to the problem must be used. In particular, analysis tools as the one based on the 3D Lomb periodogram [17], which allow to consider arbitrary distributions of coils in the (φ, ϑ) coordinates space, may be used to determine n and m. Applying the Lomb periodogram technique to the low frequency mode that appears in figure 12 provides the result shown in figure 16. Only the analysis of the perturbations along the parallel direction is shown, being very similar to the one obtained using any of the other two components.

Note that, because of how they have been deployed inside the device, both helical arrays describe a straight path in magnetic coordinates defined by $\vartheta \approx \vartheta_0 - N\varphi$, where

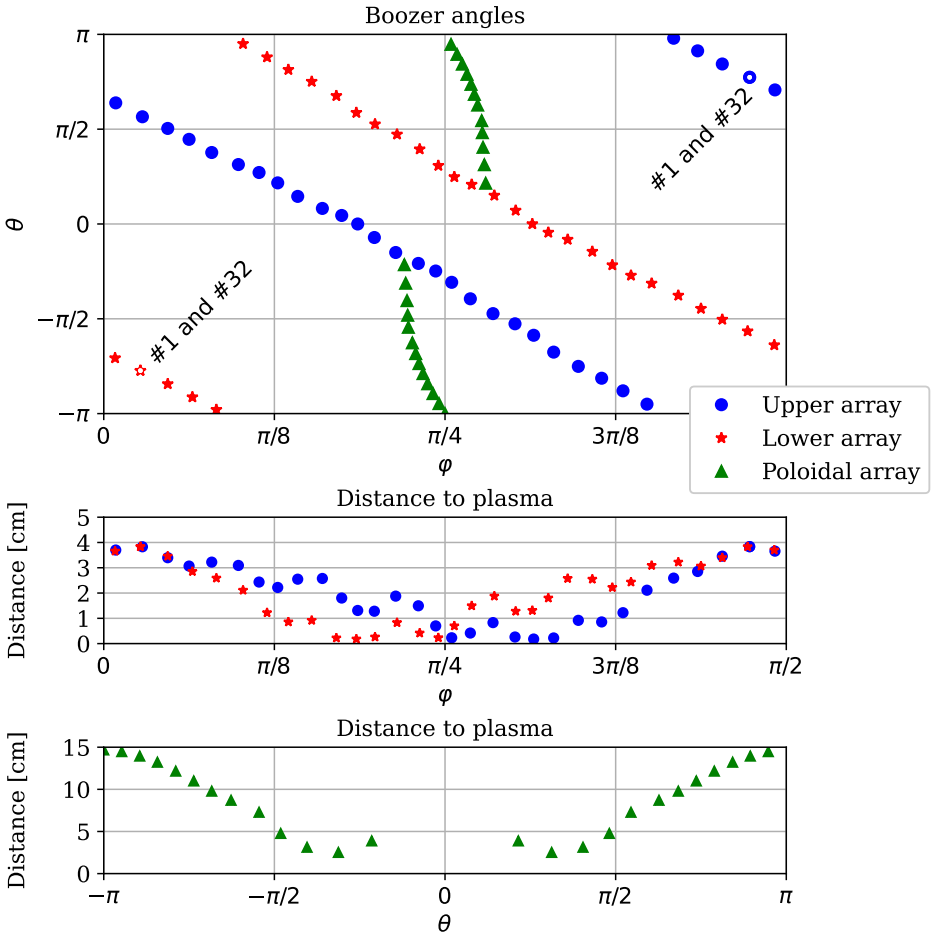

Figure 15. Mapped position in boozer angles of each set of triaxial coils for both helical arrays (blue and red dots). The coordinates of the coils of the poloidal array are also shown (green dots) illustrating the smaller variation in toroidal boozer angle. Below, the distance of the coils to the last closed flux surface is represented, along the toroidal angle φ for the upper and lower arrays, and along the poloidal angle θ for the poloidal array.

$N = 4$ is the device period and ϑ_0 the intercept, which is different for each array (see figure 15). This has an immediate consequence on the phase difference information provided by one single array. For a mode with mode numbers n and m, its spatial phase $\chi \equiv m\vartheta + n\varphi$, evaluated along any of the two arrays, is given by $\chi \approx m(\vartheta_0 - 4\varphi) + n\varphi$, and all (n, m) pairs such that $d\chi/d\varphi = n - 4m$ is constant will result in same phase differences measured between different coils and therefore will be singled out in the analysis. For the case represented in figure 16, $d\chi/d\varphi \approx 12$ and therefore $m \approx n/4 - 3$. The only pair of mode numbers which is consistent with the rotational transform of the device is $n/m = -8/-5$. The data measured by both helical arrays have been used to get the result shown in figure 16. Had we used separately any of the two arrays, we would have seen all the possible combinations of n, m values in the periodogram result. Using both arrays simultaneously helps reducing the indeterminacy. In this case, this and the

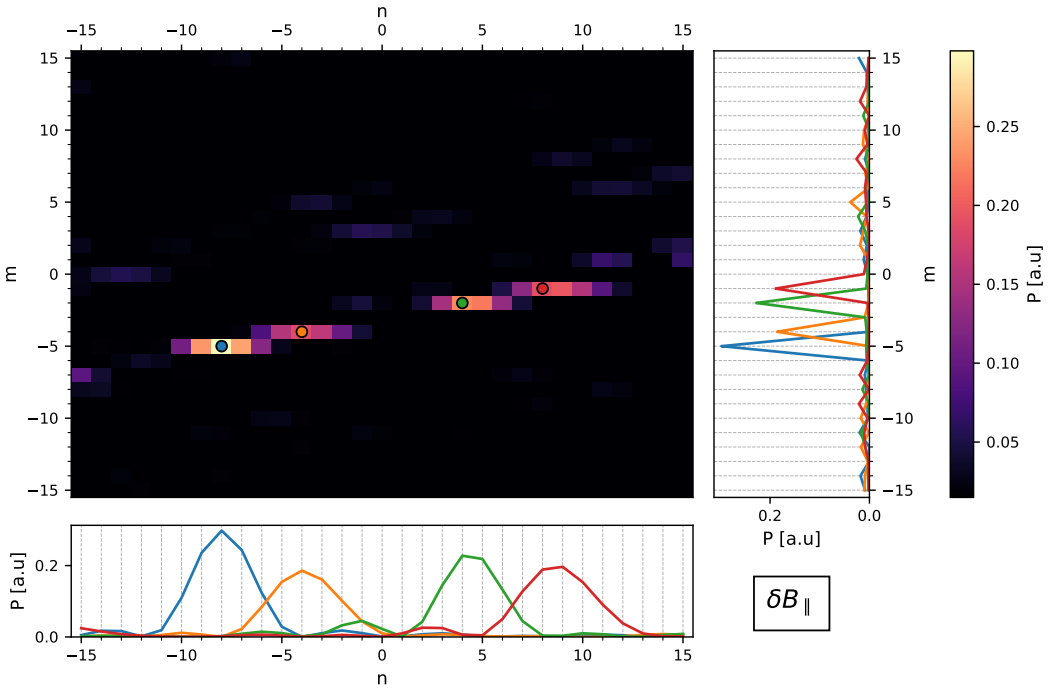

Figure 16. Central panel shows the Lomb periodogram result obtained for the low frequency mode shown in figure 12. Side panels show the periodogram amplitude along the axes determined by each (n, m) pair. In this case all pairs satisfy $m \approx n/4 - 3$.

knowledge of the available values of rotational transform narrows the possibilities to the pair of mode numbers mentioned above.

As shown in figure 15, the distance from the coils to the last closed plasma surface depends on the toroidal angle since the plasma shape suffers slight variations as it wounds around the central and helical conductors of the device. The mean of the oscillations envelope introduced in figure 13, which can be taken as a measure of the intensity of the fluctuations in each location, is represented in figure 17 against the distance that separates each set of coils from the plasma.

The amplitude of the perturbed magnetic field decays with the distance the faster the higher the mode numbers. Thus, the study of the dependence of the relative intensities of the oscillations with respect to the probe distance to the mode, whose radial location may be determined experimentally using heavy ion beam probes (HIBP) or tomographic diagnostics, might also provide useful mode number information. This is left for future work.

We now turn to another example of mode number analysis. In this case, different modes are observed during the combined injection of both co and counter neutral beams. These are identified as Shear Alfvén Waves [18] as it follows from the dependence of its frequency on line density. Figure 18 shows the spectrogram of magnetic fluctuations measured with one of the lower array coils. A rich spectrum of modes generated by both injectors appears.

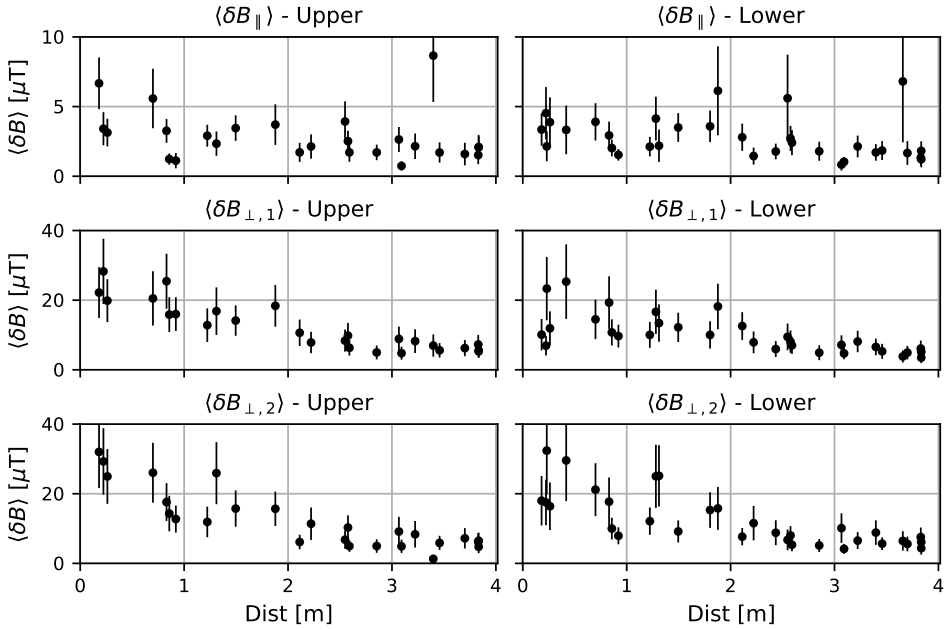

Figure 17. Mean signal amplitude represented against distance of each set of coils to the last closed flux surface, for both upper and lower arrays.

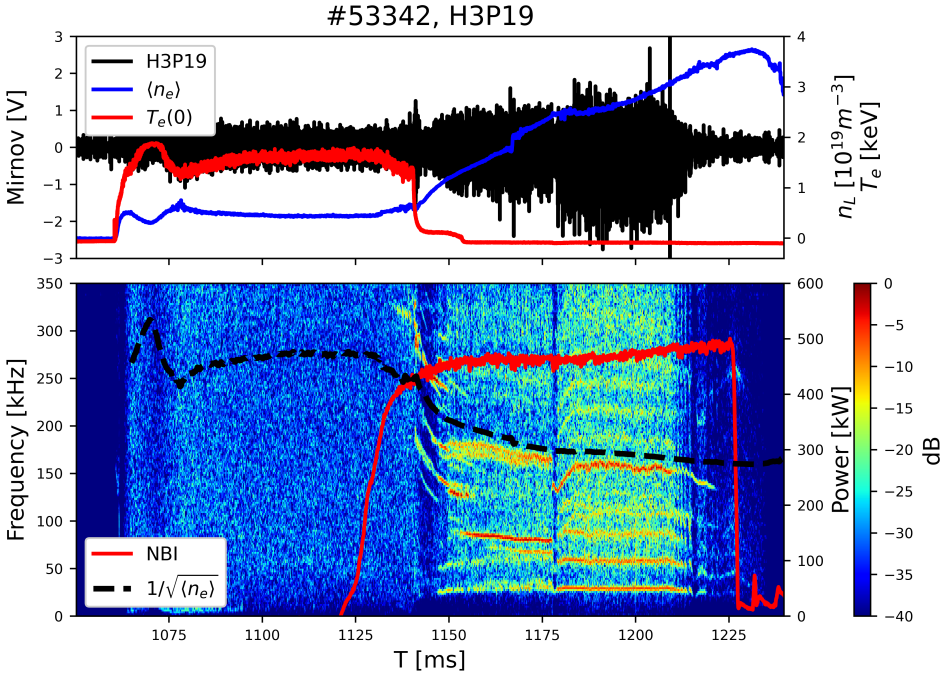

Figure 18. On top, the raw time signal of one of the lower array coils (black line) together with the line density (blue line) and the central ECE electron temperature (red line). Bottom panel shows the spectrogram of magnetic fluctuations is shown as well as the $1/\sqrt{\langle n_e \rangle}$ behaviour. Only counter-NBI power waveform is shown.

The mode number analysis is performed for the high frequency mode that appears in the interval $t \approx 1180 - 1200$ ms at $f \approx 160$ kHz. Following the previous discussion, the

analysis shows now that several values of $d\chi/d\varphi$ are present in the detected signals, where each value corresponds to a different combination of (n, m) pairs such that $n - 4m = d\chi/d\varphi$. In this case, where the mode under study is very likely an Alfvén gap mode, the interpretation of the result requires a theoretical assessment with is beyond the scope of this paper. Each of the different "branches", or straight lines with N=4 slope, actually correspond to a different mode family ($N_f = 0, 1, 2$) and to determine whether or not the measured (n, m) pairs actually correspond to helical or toroidal mode couplings needs a more thorough study that also involves poloidal mode number measurements. This is left for future work.

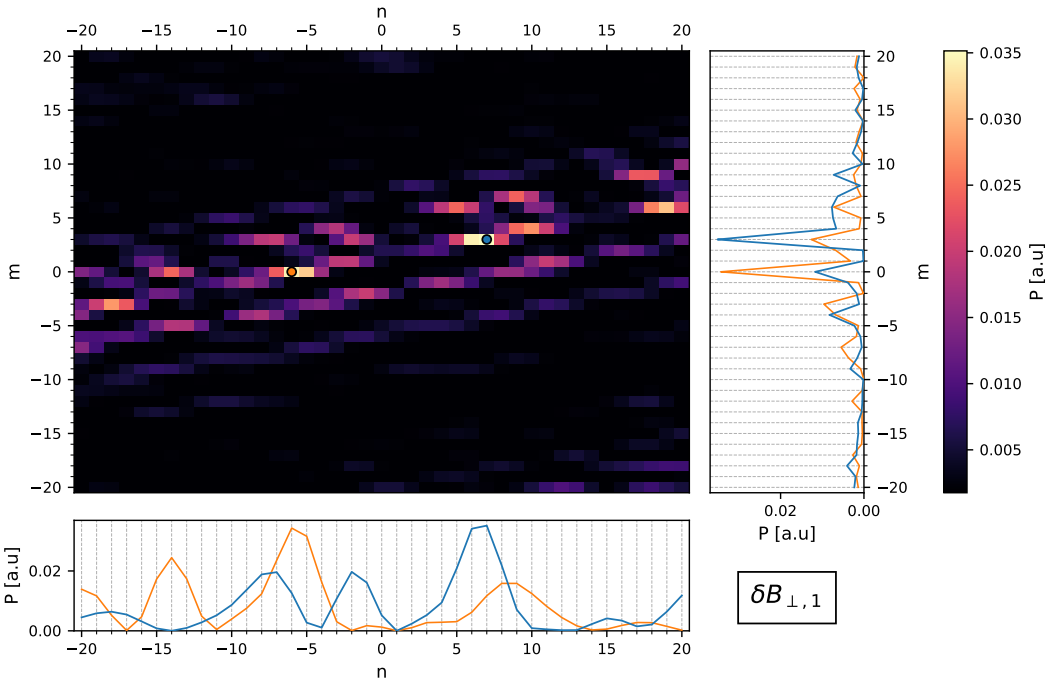

Figure 19. Central panel shows the Lomb periodogram result obtained for the high frequency mode ($f \approx 160$ kHz) shown in figure 18. Side panels show the periodogram amplitude along the axes determined by each (n, m) pair.

4. Summary

This work describes a new set of triaxial magnetic pick-up coils that has been recently installed inside the TJ-II vacuum vessel, with the main purpose of measuring the spatial periodicity of the MHD modes observed in the plasmas of this device. The design features of the coil arrays (geometry, topology, electrical parameters, supporting, positioning and installation inside the vessel) are reported in detail. The calibration procedure, intended to determine the precise orientation of each coil after its installation, is explained. As a result, we have measured the deviation of each triaxial coil from its nominal design orientation, checked its polarity and brought to light potential errors in the coils identification. This knowledge enables the mode number analysis and allows

us to investigate the amplitude decay of the perturbed magnetic field produced by a given MHD mode, which is also related to its spatial periodicity. Once properly calibrated, the triaxial setup also provides additional information on the polarization of the field perturbations. The highly 3D structure of the plasma column and the precise distribution of the coils along the toroidal direction has important consequences on the underlying phase difference information which has to be considered carefully when extracting the mode numbers of a particular perturbation. Two examples of application of this diagnostic to the identification of MHD modes are presented and discussed. The 3D Lomb Periodogram has been applied for this purpose, performing a previous mapping of the coils position to magnetic coordinates. This mapping actually reveals that the measured phase differences also depend on the poloidal mode number m, and that both helical and poloidal arrays of Mirnov coils must be used in a combined way in order to determine m and n unambiguously. The results obtained are very promising. Taking advantage of the rich spectrum of instabilities observed in TJ-II NBI plasmas, several activities related on the one hand to the development of numerical analysis tools and, on the other hand, devoted to explore new experimental scenarios, are now ongoing. Their outcome will be presented in the future.

5. Acknowledgements

The authors gratefully acknowledge the invaluable support of the entire TJ-II team. This work has been partially funded by the Spanish Ministry of Science and Innovation under several contracts, ENE2013-48109-P, FIS2017-88892-P and FIS2017-85252-R and by the European Regional Development Fund (ERDF) “A way of making Europe”. It has been also carried out within the framework of the EUROfusion Consortium under grant agreement No 633053. The views and opinions expressed herein do not necessarily reflect those of the European Commission.

References

[1] R. Jiménez-Gómez, A. Könies, E. Ascasíbar, F. Castejón, T. Estrada, L. G. Eliseev, A. V. Melnikov, J.A. Jiménez, D. G. Pretty, D. Jiménez-Rey, M.A. Pedrosa, A. de Bustos, and S. Yamamoto. Alfvén eigenmodes measured in the TJ-II stellarator. Nuclear Fusion, 51(3):033001, 2011.

[2] K. Nagaoka, T. Ido, E. Ascasíbar, T. Estrada, S. Yamamoto, A.V. Melnikov, A. Cappa, C. Hidalgo, M.A. Pedrosa, B.Ph. van Milligen, I. Pastor, M. Liniers, M.A. Ochando, A. Shimizu, L.G. Eliseev, S. Ohshima, K. Mukai, and Y. Takeiri and. Mitigation of NBI-driven alfvén eigenmodes by electron cyclotron heating in the TJ-II stellarator. Nuclear Fusion, 53(7):072004, jul 2013.

[3] A.V. Melnikov, E. Ascasibar, A. Cappa, F. Castejón, L.G. Eliseev, C. Hidalgo, P.O. Khabanov, N.K. Kharchev, A.S. Kozachek, L.I. Krupnik, M. Liniers, S.E. Lysenko, J.L. de Pablos, S.E. Sharapov, M.V. Ufimtsev, and V.N. Zenin and. Detection and investigation of chirping alfvén eigenmodes with heavy ion beam probe in the TJ-II stellarator. Nuclear Fusion, 58(8):082019, jun 2018.

[4] Á. Cappa, J. Varela, D. López Bruna, E. Ascasíbar, M. Liniers, L.G. Eliseev, J.M. Fontdecaba, J.M. García-Regaña, A. González-Jerez, N.K. Kharchev, F. Medina, A.V. Melnikov, S. Mulas, M. Ochando, D. Spong, J.L. Velasco, and TJ-II Team. Stability analysis of TJ-II stellarator NBI driven alfvén eigenmodes in ECRH and ECCD experiments. Nuclear Fusion, 61(6):066019, may 2021.

[5] S. Sakakibara, H. Yamada, and LHD Experiment Group. Magnetic measurements in lhd. Fusion Science and Technology, 58(1):471–481, 2010.

[6] M. Endler, B. Brucker, V. Bykov, A. Cardella, A. Carls, F. Dobmeier, A. Dudek, J. Fellinger, J. Geiger, K. Grosser, O. Grulke, D. Hartmann, D. Hathiramani, K. Höchel, M. Köppen, R. Laube, U. Neuner, X. Peng, K. Rahbarnia, K. Rummel, T. Sieber, S. Thiel, A. Vorköper, A. Werner, T. Windisch, and M.Y. Ye. Engineering design for the magnetic diagnostics of wendelstein 7-x. Fusion Engineering and Design, 100:468–494, 2015.

[7] K Rahbarnia, H Thomsen, J Schilling, S vaz Mendes, M Endler, R Kleiber, A Könies, M Borchardt, C Slaby, T Bluhm, M Zilker, and B B Carvalho and. Alfvénic fluctuations measured by in-vessel mirnov coils at the wendelstein 7-x stellarator. Plasma Physics and Controlled Fusion, 63(1):015005, nov 2020.

[8] M. J. Hole, L. C. Appel, and R. Martin. A high resolution mirnov array for the mega ampere spherical tokamak. Review of Scientific Instruments, 80(12):123507, 2009.

[9] R. Jiménez-Gómez, E. Ascasíbar, T. Estrada, I. García-Cortés, B. Van Milligen, A. López-Fraguas, I. Pastor, and D. López-Bruna. Analysis of magnetohydrodynamic instabilities in tj-ii plasmas. Fusion Science and Technology, 51(1):20–30, 2007.

[10] B.Ph. van Milligen, L. García, B.A. Carreras, M.A. Pedrosa, C. Hidalgo, J.A. Alonso, T. Estrada, and E. Ascasíbar. MHD mode activity and the velocity shear layer at TJ-II. Nuclear Fusion, 52(1):013006, dec 2011.

[11] S. R. Haskey, B. D. Blackwell, B. Seiwald, M. J. Hole, D. G. Pretty, J. Howard, and J. Wach. A multichannel magnetic probe system for analysing magnetic fluctuations in helical axis plasmas. Review of Scientific Instruments, 84(9):093501, 2013.

[12] A. López-Fraguas et al. Magnetic surface mapping in the tj-ii heliac. Proceedings of the 13th International Stellarator Workshop (Autralian National University-Research School of Physical Sciences and Engineering, Canberra, Australia), PI:6, 2002.

[13] Richard Everson. Orthogonal, but not orthonormal, procrustes problems. Advances in computational Mathematics, 3(4), 1998.

[14] Olga Sorkine-Hornung and Michael Rabinovich. Least-squares rigid motion using svd, 2016. Technical note.

[15] Á. Cappa et al. Nbi-driven shear alfvén waves in the presence of ecr heating and ec driven current in the tj-ii stellarator. In 28th IAEA Fusion Energy Conference (FEC 2020).Contribution ID:

962, 2021.

[16] J S Kim, D H Edgell, J M Greene, E J Strait, and M S Chance. MHD mode identification of tokamak plasmas from mirnov signals. Plasma Physics and Controlled Fusion, 41(11):1399–1420, nov 1999.

[17] Stefan Zegenhagen, Andreas Werner, Arthur Weller, and Thomas Klinger. Analysis of alfvén eigenmodes in stellarators using non-evenly spaced probes. Plasma Physics and Controlled Fusion, 48(9):1333–1346, aug 2006.

[18] Fulvio Zonca, Liu Chen, and Robert A Santoro. Kinetic theory of low-frequency alfvén modes in tokamaks. Plasma Physics and Controlled Fusion, 38(11):2011–2028, 1996.